Available online at www.sciencedirect.com
ScienceDirect
Journal of Power Sources 172 (2007) 287–295
JOURNAL OF POWER SOURCES
www.elsevier.com/locate/jpowsour

Dynamic behaviour of liquid water emerging from a GDL pore into a PEMFC gas flow channel

Xun Zhu [a], P.C. Sui [b], Ned Djilali [b,*]

[a] *Institute of Engineering Thermophysics, Chongqing University, Chongqing 400044, China*
[b] *Institute for Integrated Energy Systems and Department of Mechanical Engineering, University of Victoria, Victoria, BC V8W 3P6, Canada*

Received 1 June 2007; received in revised form 4 July 2007; accepted 4 July 2007
Available online 19 July 2007

Abstract

A numerical investigation of the dynamic behaviour of liquid water entering a polymer electrolyte membrane fuel cell (PEMFC) channel through a GDL pore is reported. Two-dimensional, transient simulations employing the volume of fluid (VOF) method are performed to explicitly track the liquid–gas interface, and to gain understanding into the dynamics of a water droplet subjected to air flow in the bulk of the gas channel. The modeled domain consists of a straight channel with air flowing from one side and water entering the domain from a pore at the bottom wall of the channel. The channel dimensions, flow conditions and surface properties are chosen to be representative of typical conditions in a PEMFC. A series of parametric studies, including the effects of channel size, pore size, and the coalescence of droplets are performed with a particular focus on the effect of geometrical structure. The simulation results and analysis of the time evolution of flow patterns show that the height of the channel as well as the width of the pore have significant impacts on the deformation and detachment of the water droplet. Simulations performed for droplets emerging from two pores with the same size into the channel show that coalescence of two water droplets can accelerate the deformation rate and motion of the droplets in the microchannel. Accounting for the initial connection of a droplet to a pore was found to yield critical air inlet velocities for droplet detachment that are significantly different from previous studies that considered an initially stagnant droplet sitting on the surface. The predicted critical air velocity is found to be sensitive to the geometry of the pore, with higher values obtained when the curvature associated with the GDL fibres is taken into account. The critical velocity is also found to decrease with increasing droplet size and decreasing GDL pore diameter.

Keywords: Water droplet dynamics; Hydrophobic; Surface tension; Fuel cell; Gas diffusion layer; Water management

1. Introduction

Water management is central to achieving performance and durability of low temperature PEMFCs. In an operating PEMFC, water is often introduced into the cell through humidified reactants and is also produced in the catalyst layer on the cathode side. Since in most designs liquid water shares the same flow passages with the reactants, when liquid water is not removed from the cell at a sufficient rate, partial blockage of the pathways takes place, leading eventually to so-called flooding. Liquid water saturation of the GDL pores reduces transport of reactant gases [1], and may lead to complete starvation. In addition to performance losses this can also induce local cell reversals, exacerbate degradation [2] and compromise cold start operation. The emergence of the excess liquid water into the gas channels can induce a significant additional pressure drop, as well as local blockage of gas channels that results in global flow maldistribution. *In situ* observations and measurements of liquid water transport in an operating unit cell is challenging, and understanding of the dynamics of two-phase flow in the cathode microchannels remains thus limited. The flow and surface conditions encountered in PEMFC microchannels result in flow regimes that are generally different from those encountered in more classical engineering applications, because of the small hydraulic diameters ($\sim$500 μm), low Reynolds numbers ($\sim 10^3$ or less) and mixed wetting properties of the surfaces. The resulting microscale flows in PEMFCs are for the most part laminar and are characterized by much larger ratios of surface to volume forces.

* Corresponding author.
E-mail address: ndjilali@uvic.ca (N. Djilali).

0378-7753/$ – see front matter © 2007 Published by Elsevier B.V.
doi:10.1016/j.jpowsour.2007.07.024

In particular surface tension and viscous forces become predominant. Thus most of the knowledge in the rich literature on two-phase flow in channels is not readily applicable to PEMFCs.

A few studies have been undertaken in recent years targeting specifically two-phase flows in PEM fuel cells using transparent fuel cell hardware [3–8], neutron scattering imaging [9–12], IR-thermography [13], NMR [14], MRI [15] and fluorescence microscopy [16,17]. In custom made cells with an optically accessible window, flow phenomena including droplet formation, flow regimes, and scenarios of droplet–droplet and droplet–wall interactions can be observed and often quantified using image processing techniques. However, the materials used for transparent windows typically have different bulk properties (thermal and electrical) and surface properties (roughness and wettability) from those in actual fuel cells, thus dictating a certain amount of caution in interpreting the observations. Techniques such as neutron or magnetic resonance imaging circumvent the need for an optically transparent window but require materials and/or cell designs that differ significantly from those of operating systems. These promising techniques require further advances to enhance their practicality as well as temporal and spatial resolution.

Most modeling and simulations of water transport in fuel cell have to date focused on water flow in the porous components of the cell, e.g., water saturation and capillary transport in the GDL [18–23] and transport of absorbed water in the ionomer phase [24–26]. These studies assume, explicitly or implicitly, that water appears as a homogeneous phase within the representative volume. This approach cannot be extended to the analysis of liquid water transport in a gas microchannel where large liquid interfaces are expected as a result of strong interactions between surface tension and the channel walls. Simplified stability analysis based on macroscopic force balances and geometry approximations have been reported in Chen et al. [27], Jiao et al. [28], Quan et al. [29] and Kumbur et al. [30]. In these studies, a single droplet or an array of droplets are considered to be either suspended in the channel, attached to the channel wall, or in the form of a water film. None of these studies accounts for the facts that in a PEMFC liquid water emerges from the GDL pore into the gas channel, as well as the fact that GDL pores are constructed by intersecting carbon fibres which impart curvature to the pore outlet into the channel. Key questions that remain from the view point of design are understanding of the dynamics of liquid water droplets; of the detachment process and ensuing entrainment and interaction with the channel walls and other droplet; and the characterization of the pressure drop. We recently reported on a numerical study of the dynamic behaviour of a water droplet emerging from a pore into a microchannel [31]. In that work we examined the impact of surfaces of varying wettability, and the effects of static contact angle, air velocity, and water velocity, and presented an analysis of the critical air inlet velocity. In the present study, we focus on emergence of water onto a hydrophobic surface, corresponding to a PTFE treated GDL, and extend the volume-of-fluid dynamic model to specifically account for salient geometric features of the pores through which water emerges. We track and document the complete droplet emergence and formation process as well as the subsequent detachment and/or film formation, and also present some results on the dynamic interaction of two droplets emerging from separate pores. A parametric study on the critical air inlet velocity at which detachment and removal of water droplet from the microchannel is induced is presented. Implications of the present findings on PEMFC operation are also discussed.

2. Numerical model and VOF method

The volume-of-fluid (VOF) method employed in the present study was first developed in the early 1980s [32] and has become a popular technique for direct numerical simulation of time-dependent flows of immiscible fluids. In VOF methods, the location of the interfaces is determined by applying a surface-tracking technique to a fixed Eulerian mesh and can thus be readily implemented into a CFD framework. A volume fraction indicator is used in conjunction with a reconstruction technique to determine the location and shape of the interface. A key feature of the VOF method is the ability to capture the effects of surface tension, which is an important and sometimes dominant force in microchannel flows, using a continuum surface force approach.

2.1. Numerical method

Unsteady, isothermal laminar flow conditions are assumed to prevail for both air flow and water droplet motion inside the microchannel, since the bulk flow Reynolds number is less than 650 [33,34] and the heat generation and heat transfer are negligible. The two-dimensional numerical model was implemented using the commercial CFD package, FLUENT 6.3, and the volume of fluid (VOF) method was employed in conjunction with an interface reconstruction algorithm to track the dynamics of the deforming water droplets [35].

In the VOF technique, a single set of momentum equations is shared by both fluid phases, and the interface between phases is tracked for each computational cell throughout the domain by computing the volume fraction for the fluid k:

$$C_k(x, y, z, t) = \begin{cases} 0 & \text{(outside } k\text{th fluid)} \\ 1 & \text{(inside } k\text{th fluid)} \\ 0 \sim 1 & \text{(at the } k\text{th fluid interface)} \end{cases} \quad (1)$$

where C_k is the volume fraction function of kth fluid, and the sum of the volume fraction functions is equal to 1.

$$\sum_{k=1}^{n} C_k = 1 \quad (2)$$

C_k is governed by a volume fraction equation [35] which is solved in every computational cell:

$$\frac{\partial}{\partial t}(C_k \rho_k) + \nabla \cdot (C_k \rho_k \vec{u}_k) = 0 \quad (3)$$

The velocity field for the two-phase mixture in the microchannel is governed by the Navier–Stokes equation:

$$\frac{\partial}{\partial t}(\rho\vec{u})+\nabla\cdot(\rho\vec{u}\vec{u})=-\nabla p+\nabla\cdot[\mu(\nabla\vec{u}+\nabla\vec{u}^{\mathrm{T}})]+\rho\vec{g}+\vec{F} \quad (4)$$

where p is the static pressure, $\vec{F}$ a momentum source term related here to surface tension, and ρ and μ are the volume averaged density and dynamic viscosity. These are computed to account for the variable volume fractions for the two-phase air–water system considered here:

$$\rho = \rho_1 + C_2(\rho_2 - \rho_1) \quad (5)$$

$$\mu = \mu_1 + C_2(\mu_2 - \mu_1) \quad (6)$$

where indices 1 and 2 represent air and water, respectively.

Surface tension is accounted for by using the continuum surface force (CSF) model [36], and is expressed in terms of the pressure jump across the interface, which depends on the surface tension coefficient, and is implemented in the momentum equation as a body force $\vec{F}$:

$$\Delta p = \sigma\frac{1}{R} \quad (7)$$

$$\vec{F}_{\mathrm{vol}} = \sigma\kappa_k\frac{\rho\nabla C_k}{1/2(\rho_1+\rho_2)} \quad (8)$$

where Δp is the pressure jump across the surface, σ the surface tension coefficient, and R is the surface curvature radii. The curvature κ_k is computed from local gradients in the surface normal at the interface.

$$\kappa_k = \nabla\cdot\left(\frac{n}{|n|}\right) \quad (9)$$

and the surface normal n is defined as the gradient of C_k, the volume fraction of the kth phase.

$$n = \nabla C_k \quad (10)$$

2.2. Computational domain and mesh

Fig. 1 shows a schematic of the computational domain and the corresponding mesh. In this study, the problem is simplified by assuming two-dimensionality. In the simulations, the channel in the base line case is 250 μm high and 1000 μm long with an injection pore of width $D = 50$ μm. These dimensions are representative of gas flow channels used in PEM fuel cells, and the pore widths considered are typical of values observed in microscope images of gas-diffusion layers (GDL) [16]; the length of channel simulated is relatively small due to the very high computational costs but sufficiently large to resolve the initial dynamics which is the focus of his work. Air flow enters the channel from the left side at a velocity U. Water with a velocity V enters the channel through the pore on the bottom surface. This scenario simulates the transport into the channel of water produced by the electrochemical reaction. The fixed location of the GDL pore is consistent with experimental observation that indicates water usually appears preferentially on certain site of the GDL surface [16,17]. A structured orthogonal computational mesh consisting of 15,810 cells is used for the base line case. The adequacy of this grid was tested by increasing and decreasing the number of grid nodes by ±20%, and similar water droplet transport and deformation processes were obtained with all three grids.

2.3. Boundary and initial conditions

Uniform velocity profiles are specified at both air channel and water inlet respectively, cf. Fig. 1. A convective outflow condition is applied at the channel outlet. A no-slip boundary condition is imposed along the walls of the channel. A surface tension of 0.0725 N m^{-1} is prescribed for all cases. A static contact angle of 140° is used for the GDL surface unless otherwise stated. The wall of the channel other than the GDL surface is set to be hydrophilic with a static contact angle of 45°. These values of static contact angle, or surface wettability, are typical for PEMFC materials. We note that the static contact angle is a measure of surface wettability, which is obtained for water in a stagnant environment at low Bond number ($Bo = \rho g d^2/\sigma$), and is thus specified as a boundary condition in the problem formulation. The actual contact angle at the liquid/gas/solid interface is the result of the net balance (or imbalance if the volume of water is in motion) of the aforementioned forces in the vicinity of the triple phase boundary. All calculations reported in this paper begin with an initial field consisting of air flowing with a uniform velocity. An air velocity of 10 m s^{-1} at a pressure of 1 bar and temperature 298 K is used. This air velocity is of the same order of magnitude as the cathode flow velocities in a typical operating PEM fuel cell at high current density conditions. The velocity of water entering the channel is taken as 1 m s^{-1} in the simulations.

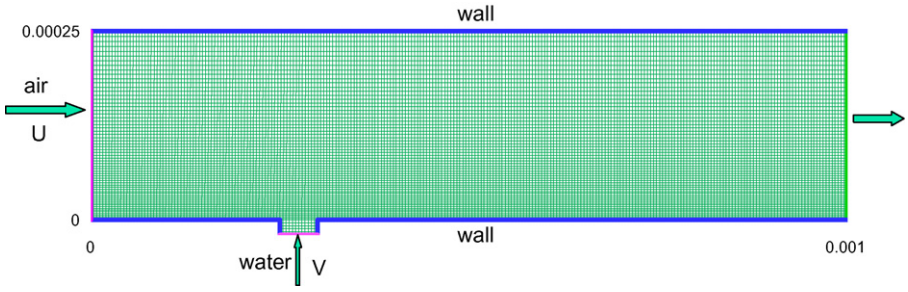

Fig. 1. Computation domain and mesh for the 2D VOF simulations.

3. Results and discussion

The dynamics of a blob of water emerging from the bottom surface of a microchannel and subjected to a cross air stream are affected by several factors including: (1) channel dimensions, channel geometry, and GDL pore size, (2) flow conditions, and (3) surface properties. The shape and motion of a blob of water are determined by the combined effects of shear stress, inertia force, surface tension, pressure, gravity, and viscous force. Some pertinent dimensionless numbers that represent the ratio of surface tension to the other forces are the capillary number ($Ca = \mu u/\sigma$), Weber number ($We = \rho u^2 d/\sigma$), and Bond number ($Bo = \rho g d^2/\sigma$). For the baseline conditions in the present study, and using the water injection pore size D as the characteristic length, we have $Ca = 1.5 \times 10^{-2}$, $We = 0.7$ and $Bo = 4 \times 10^{-4}$. The relatively small values of Ca and Bo indicate that surface tension is more influential than viscous and gravitational forces for the microchannel flow conditions considered. It should be noted that the surface properties, e.g., wettability and roughness, of the channel wall and the GDL surface do not manifest themselves directly in these dimensionless number, though they clearly play an important role in determining the actual dynamics of the two-phase flow.

In presenting the results, we first examine and discuss the characteristics of liquid water flow in the microchannel for the baseline case. A parametric study will then be presented to gain insights on the impact of several geometric factors on flow patterns and flow regimes. The implications of water motion on the operation of PEMFCs will finally be discussed in terms of the critical air velocity.

3.1. Characteristics of liquid water movement in a microchannel

The time evolution of an emerging water droplet for a hydrophobic GDL surface is shown in Fig. 2. Several characteristic patterns in the process of the droplet formation are identified as (1) droplet growth (a and b), (2) droplet elongation (c and d), (3) droplet collapse and wall attachment (e and f), (4) recoil and film flow (g and h). Fig. 3 shows in a compact form the results presented in Fig. 2 by superimposing the water droplet interface at different times. The emergence of the water from the pore into the channel and the gradual formation of a droplet are clearly tracked in Fig. 2(a and b). At the early stage of the process, surface tension is dominant and maintains the shape of the blob of water close to circular. As time progresses, the air flow upstream is gradually obstructed by the growing water droplet, cf. Fig. 2(c and d). As the blockage increases, the

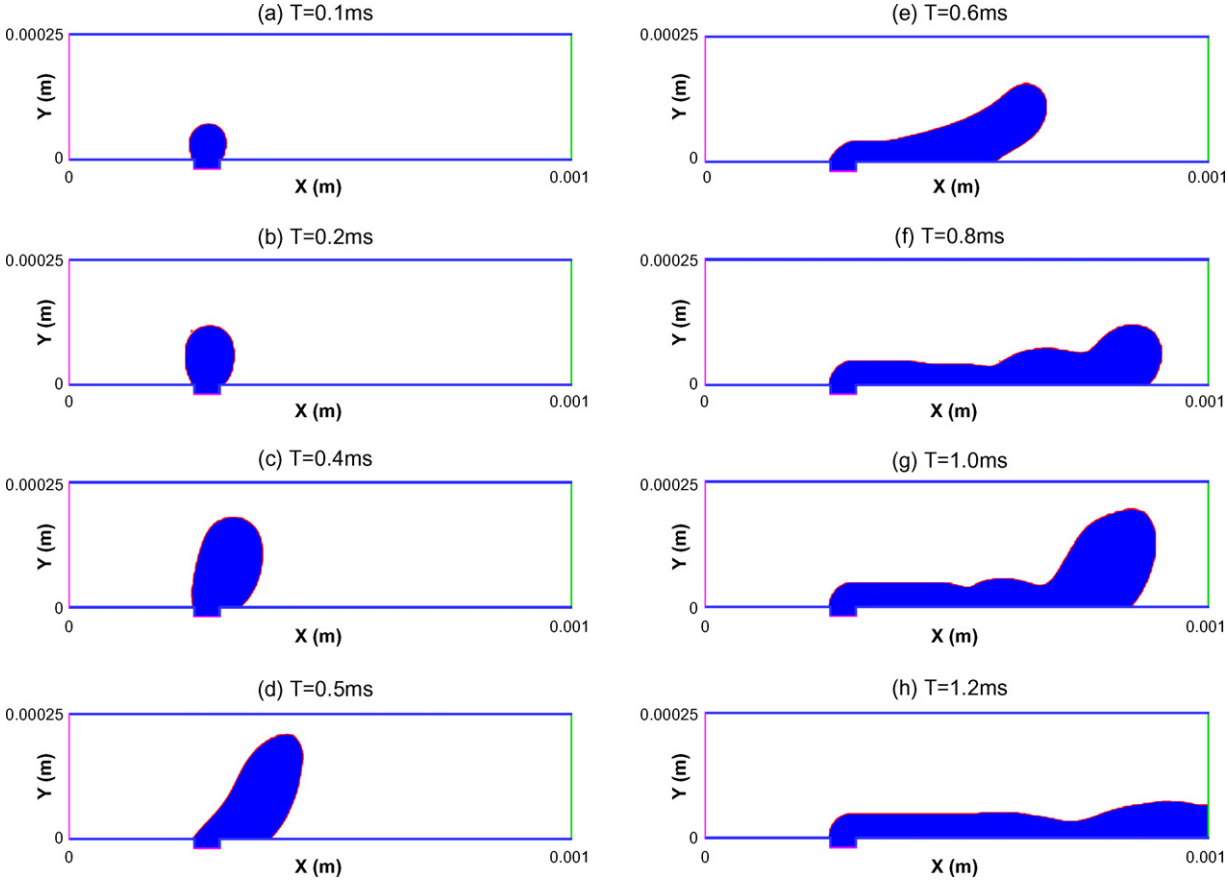

Fig. 2. (a–h) Time evolution of a water droplet emerging from a 50 μm GDL pore in a 250 μm microchannel; air flow velocity $U = 10\,\mathrm{m\,s^{-1}}$, water injection velocity $V = 1\,\mathrm{m\,s^{-1}}$.

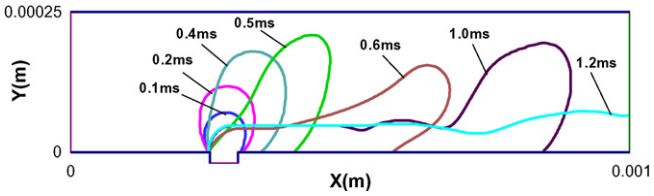

Fig. 3. Evolution of water droplet shape corresponding to the cases shown in Fig. 2.

air flow is first accelerated through the narrow gap between the droplet and the top wall, and then decelerated as illustrated in Fig. 4(a). The adverse pressure gradient downstream of the minimum gap, see Fig. 4(b), causes separation of the air flow, and a recirculation zone behind the droplet forms as a result. The pressure drop between the upstream and downstream sides of the water droplet builds up, especially at the base of the droplet, which together with the higher shearing stress on the top of the droplet destabilizes and deforms the droplet. As the volume and mass of the water droplet increase, the gravitational force on the droplet also increases while inertial force decreases due to the increasing surface area. In order to balance these forces and maintain a continuous interface, the water droplet deforms allowing adjustment of the interface curvature radii, cf. Fig. 2(e). The contact line moves rapidly downstream to form a film flow, and eventually starts rolling up, see Fig. 2(f). The air velocity decreases as the droplet attaches to the wall and channel blockage is reduced, while surface tension restores a more circular droplet shape downstream, Fig. 2(g). Following the roll-up, blockage with increased gap velocity and pressure drop becomes dominant again, however, in this phase the air flow and pressure fields are not as strongly affected as in Fig. 2(d), and the effect of surface tension on the droplet is relatively higher. Therefore, water droplet gradually spreads downstream and results in a film flow, cf. Fig. 2(h).

3.2. Effect of channel size

The geometry and dimension of the gas channel are critical for the performance of PEMFC. The dimensions of the channel are primarily determined based on the pressure drop requirement of the balance of plant (BOP). As is discussed previously, the narrowing gap between water droplet and the channel wall creates a strong shear stress and causes a pressure gradient on

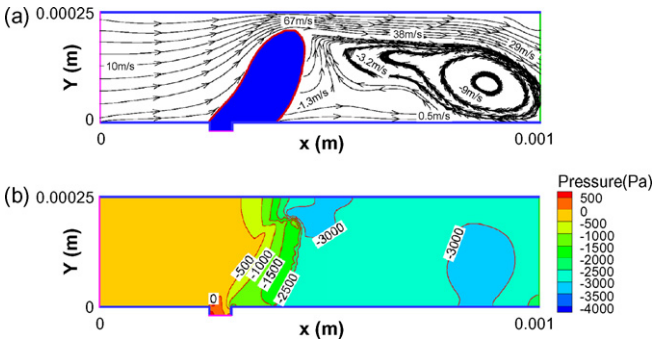

Fig. 4. (a) Flow field at $t = 0.5$ ms and (b) pressure field.

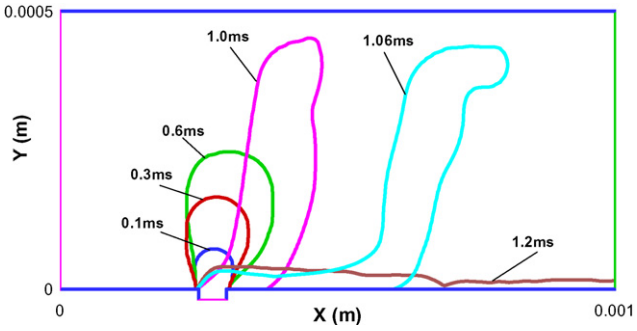

Fig. 5. Time evolution of a water droplet in a 0.5 mm height channel.

the droplet, both favoring removal of water from the GDL pore where it enters the channel. Fig. 5 shows the time evolution of a water droplet emerging into a channel with a 500 μm height. The flow conditions and surface properties of this case are identical to those shown in Fig. 3. One can see in Fig. 5 that a higher channel provides more space for the water droplet to grow up and therefore, the area blocked by the water droplet is smaller, the air flow field is more uniform, and the shearing stress and pressure difference on the interface of the water droplet are relatively weaker. Thus the water droplet grows under the dominance of surface tension and inertial force at early time ($t = 0.1$ ms, 0.3 ms, 0.6 ms), and the three phases contact line moves downstream slowly. As the water droplet grows, the shearing stress and static pressure difference increase and the water droplet deforms downstream ($t = 1$ ms, 1.06 ms). Thereafter, the water droplet attaches to the GDL surface and its front become thinner with large face to bear the static pressure difference ($t = 1.06$ ms). The film flow is formed finally ($t = 1.2$ ms) without breaking away.

3.3. Effects of pore size

The micro-structures of GDL materials are highly anisotropic and are characterized by a range of pore diameters [16]. Moreover, the pore size on the GDL surface can be altered during fabrication by changing the density of carbon fibre on the surface as well as by adjusting the PTFE treatment. Because the water produced by the electrochemical reaction in the catalyst layer transports through a range of pore sizes into the gas channel, the size of the GDL pore can potentially be used as a means of controlling the water removal capability of a GDL. Figs. 6 and 7 show the time evolution of water entering the channel through pore width of 25 and 10 μm, respectively. The conditions used in both cases are identical to those in the baseline except the pore size where water enters the channel. Compared with the baseline case in Fig. 3, the growth and deformation of the water droplet appear to be similar in the early stage, except that a longer period is needed in the case with pore width of 25 μm, cf. $t < 1.2$ ms in Fig. 6(a). For the 25 μm pore case, for $t > 1.2$ ms, the horizontal component of the surface tension is insufficient to counteract the shear and pressure forces acting on the water droplet, and consequently break up of the water droplet occurs, cf. $t = 1.4$ ms in Fig. 6(b). As time proceeds, the break-away water droplet moves downstream following the air flow with a shrinkage of its

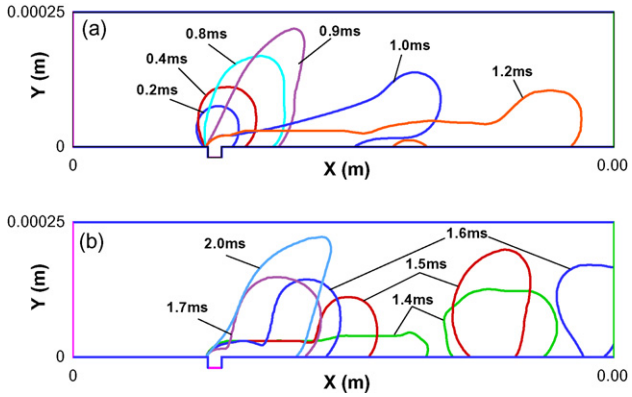

Fig. 6. Time evolution of a water droplet emerging from a 25 μm GDL pore: (a) initial phase and (b) post break-up phase.

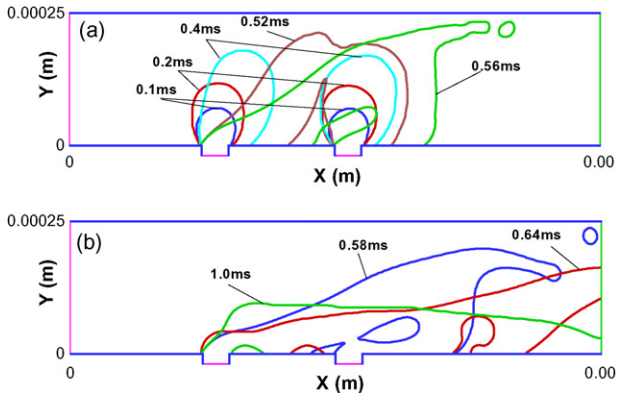

Fig. 8. (a and b) Time evolution of two coalescing water droplets emerging from separate pores.

attachment interface to the GDL surface due to hydrophobicity, while the water left behind rolls upstream and relaxes to a quasi circular droplet shape dominated by surface tension. Similar scenarios of droplet deformation recur subsequently. For an even smaller pore size, e.g., 10 μm in Fig. 7, the water droplet grows very slowly due to the smaller water volume flux and retains a relatively stable shape as time progresses.

3.4. Effects of coalescence of water droplets

In an operating PEMFC, water droplets emerge into the gas channel from various locations in the GDL, and when a water droplet detaches from the GDL pore and is convected by the air flow, it may encounter other water droplets downstream. As an initial step to mimic this process, simulations of two water droplets from two pores of the same size located 250 μm apart are performed to examine the dynamic interaction of water droplets. The growth, deformation, and coalescence stages of the two water droplets are shown in Fig. 8. Both droplets enter the channel at the same time ($t = 0$), and initially each grows similarly to a single droplet. Shortly after this stage, a remarkable deformation occurs on the upstream water droplet first, and its three-phase contact line is driven by shear stress and pressure from air flow and moves downstream at $t = 0.4$ ms; the corresponding deformation of the downstream water droplet is much less pronounced. Coalescence of the two droplets is initiated near the top interfaces of both droplets at $t = 0.52$ ms. The large water volume concentration resulting from the coalescence induces a substantial blockage of the channel flow. The air flow is accelerated through the correspondingly decreasing gap between the water droplet and the top wall, and higher shear stress therefore results on the interface. A large pressure drop along the flow direction is induced by the sudden coalescence and increased blockage. The coalescence also yields momentum transfer from the upstream droplet to the downstream one. The overall effect is an increase in body and surface forces and acceleration of the deformation process, especially near the top of the coalesced droplet, see $t = 0.56$ ms in Fig. 8(a). Moreover, the air flowing between the two water droplets is entrapped at the beginning of the coalescence and forms a bubble ($t = 0.58$ ms and 0.64 ms). Eventually, the water is removed from the channel by the air flow and a film flow regime is established. In comparison to the single droplet case, the time scale for water removal is much shorter when droplet coalescence occurs in the microchannel.

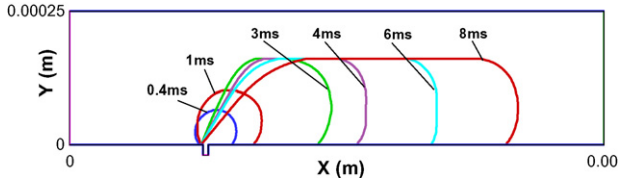

Fig. 7. Time evolution of water droplet emerging from a 10 μm GDL pore.

3.5. Critical air inlet velocity for detachment

Removal of water from the gas channel and the GDL is essential to preventing build up of water saturation and flooding and avoid transport limitation of the reactants to the catalyst sites [1]. Passive removal of water by the air flow is advantageous. However, the air stream may not be effective in achieving this under certain conditions, e.g., at low current density conditions when the air velocity is not sufficiently high to blow out the water droplets. Determination of the critical air inlet velocity at which detachment of water from the GDL pore occurs is therefore of great interest to practical fuel cell design and determination of appropriate operating conditions. This is investigated here by examining in particular the effects of the GDL pore structure and pore size on this critical velocity.

In addition to air velocity, GDL surface wettability and the shape of the droplet, the detachment of water from a GDL pore may also depend on how the droplet is pinned to the GDL surface. Most GDLs currently used in PEMFCs are fabricated from carbon fibres, which typically have diameters of 5–10 μm. The pores on the GDL surface through which water enters the gas channel are formed by such intersecting and overlapping layers of carbon fibres. It is therefore more likely that liquid water emerges into the channel following a curved edge rather than a right angle edge.

The critical air inlet velocity, U_{cr}, above which the air flow induces break away of the water droplet, is computed in the following simulations to assess the effects of the fibre structure

and the pore size. The influence of the connectivity of the water droplet to the water in the pore and the sensitivity of the presence of a fibre are investigated by performing the simulation with water emerging into channel from a pore with an arc near the GDL surface, as opposed to the case for a single stagnant water droplet sitting on a channel surface without a pore. In these simulations, we consider a water droplet of a specific equivalent diameter, d_H, defined as the diameter of a circular shape droplet having the same volume, attached to the water inside a pore and vary the air flow velocity at the channel inlet. The simulations begin with initial conditions which are obtained from a specific time step for a water droplet emerging from a pore of width 50 μm, with a velocity of 1 m s^{-1} and zero air velocity at the channel inlet. The subsequent simulation proceeds with no additional water entering the computational domain. The shape of the droplet at the beginning depends on the pore structure and surface wettability, but the total volume is the same for the same equivalent droplet diameter. Fig. 9 shows the variation of the dimensionless droplet height, which is normalized by the height of the channel, as a function of the dimensionless equivalent droplet diameter. The height of the initial droplet basically increases with increasing equivalent droplet diameter and only differs slightly for the three different configurations. For the case of water emerging from a pore with right angle edge (Fig. 9(a)), the droplet height is almost identical to that of a stagnant droplet and only a slightly higher height at the larger droplet equivalent diameter is noted. The droplet height for this case is slightly higher than that with an arc edge mimicking the structure of a fibre 10 μm in diameter, cf. Fig. 9(b). This is because the water droplet becomes shorter and wider due to the arc edge of the fibre. Fig. 10 shows the critical air inlet velocity as a function of the equivalent droplet diameter for the three cases shown in Fig. 9. For the case of a stagnant droplet sitting on a flat surface without a GDL pore, the critical air inlet velocity is relatively insensitive to the initial droplet diameter, showing less than 30% decrease for the larger droplet sizes. For the cases of a droplet initially connected to a pore, the critical air inlet velocity is much higher overall and decreases with increasing droplet size. This is consistent with the balance of the forces acting on the droplet discussed previously, in particular the result of weaker surface tension for a larger radius of curvature. A larger droplet also results in higher channel blockage, accelerating the air flow and inducing a higher streamwise pressure difference and a larger drag force. It is instructive to consider these results in relation to the simpler but related case of a circular cylinder (equivalent to a 2D circular droplet) placed in a channel. Chakraborty et al. [37] considered this problem for Reynolds numbers in the range considered here. They found that the drag coefficient ($C_D = F_{drag}/(0.5\,\rho U^2 d_H)$) decreases with Reynolds number, but increases with blockage ratio (d_h/H) due to the interplay between frictional and pressure drag. In the context of the present problem, for a droplet diameter of 98 μm, $U_{crit} \approx 5$ m s^{-1}, we have $Re \approx 31$ and the blockage ratio $d_h/H \approx 0.39$; whereas for a droplet of 187 μm, $U_{crit} \approx 3.5$ m s^{-1}, giving $Re \approx 41$ and $d_h/H \approx 0.75$; the slight decrease in the critical velocity for the larger droplet indicates a net effect of a slightly lower drag coefficient. The small change is qualitatively consistent with the results of Chakraborty et al. [37]. In the case of the droplet attached to a pore, the surface tension plays a greater role and the simpler "circular cylinder" analysis does not apply. As shown in Fig. 10, the critical velocity for droplets attached to either shape of pore are initially much larger than for the droplet on the surface, and drop significantly with increasing droplet size. The critical air velocity for the case with an rounded pore edge is overall higher than the case with a right angle edge except for $d_H < 100$ μm. This can be explained by noting that the arc fibre edge helps maintain the stability of the water droplet and result in less deformation by surface adhesion due to the gradual change in the surface orientation. The shear stress and pressure forces are thus lower, and a higher critical air inlet velocity is therefore required in order to break the connection of the water droplet to the water inside the pore.

Fig. 11 shows the dimensionless droplet height as a function of equivalent droplet diameter for water emerging from three different pore width: 50, 25 and 10 μm. The droplet heights are very similar in all three cases, and the slight decrease in the slope shows a gradual reduction of the droplet aspect ratio for larger droplets. The critical air inlet velocity decreases monotonically with increasing droplet equivalent diameter as expected, and

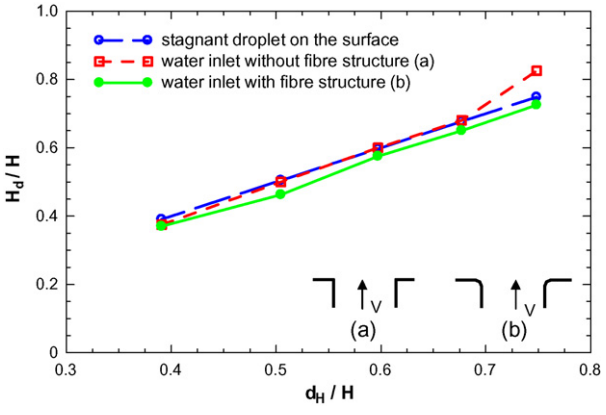

Fig. 9. Variation of dimensionless droplet height equivalent droplet diameter for sharp edge pore and rounded edge pore geometries.

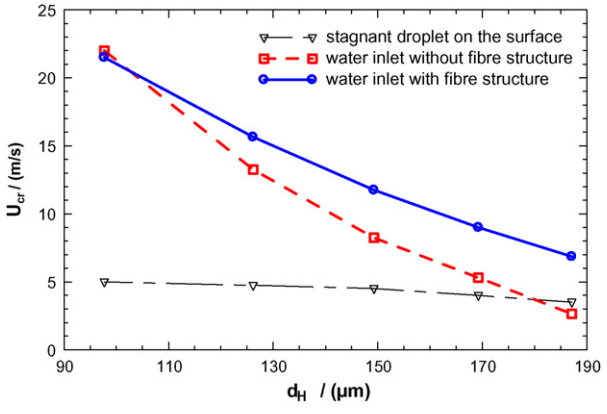

Fig. 10. Variation of critical air inlet velocity as a function of equivalent droplet diameter and comparison of predictions including droplets initially pinned to a pore and droplet initially stagnant on flat surface.

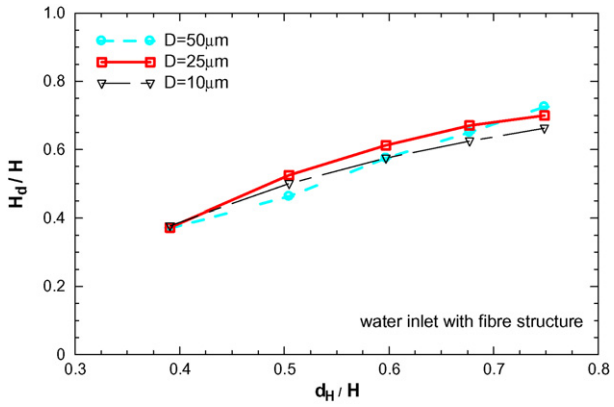

Fig. 11. Variation of dimensionless droplet height with equivalent droplet diameter for different pore sizes.

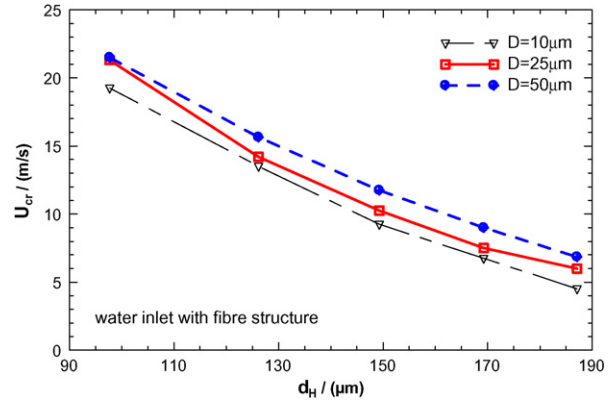

Fig. 12. Critical air inlet velocity as a function of equivalent droplet diameter. Predictions obtained using curved pore outlet accounting for fibre structure on the GDL surface.

shows a small but noticeable dependence on pore width as shown in Fig. 12, with droplets emerging from small pores detaching at lower velocities. In an actual PEMFC, a range of effective pore sizes as well as a range of droplet sizes will be present on the GDL surface. Based on the present findings it is therefore expected that under the same air velocity in the gas channel, some water droplets will detach and move out of the channel while others will remain pinned. Other factors, such as pore structure and droplet volume, may also play a role in the water eruption mechanism [16] and the associated growth rate of the water droplet.

4. Conclusions

A numerical investigation on the dynamic behaviour of a water droplet emerging from a single pore into a straight microchannel was presented using a two-dimensional model in conjunction with the volume of fluid (VOF) method. The effects of the gas channel size, coalescence of droplets, and pore size on the water droplet dynamics were investigated, documenting in particular the critical air inlet velocity at which droplet detachment occurs and the effect of the connectivity of the water inside pore as well as the curvature of the edge of pore. The main findings and conclusions are summarized below.

(1) A water droplet emerging onto the hydrophobic surface (GDL) of a fuel cell channel and its interaction with the air flow yields a complex pattern of droplet growth, deformation, collapse and wall attachment, breakup, recoil and eventual film formation.
(2) In large microchannels, the downstream deformation of the water droplet slows down and droplet breakup may not occur.
(3) Coalescence of two water droplets accelerates deformation and liquid water motion in a microchannel.
(4) The critical air inlet velocity predicted taking into account the connectivity of water to the pore is much higher than those reported in previous works considering processes starting from a stagnant droplet sitting on the GDL surface. Furthermore, a higher critical air velocity is predicted when taking into account the curvature of the pore.
(5) For the same initial droplet size, the critical air velocity decreases with decreasing pore width.

While the present 2D simulations provide some rich insights, it should be noted that a complete representation of some of the dynamic processes requires three-dimensional simulations. These computationally intensive simulations are planned for future work.

Acknowledgements

X.Z. is grateful for the support by the National Natural and Science Foundation of China (No. 90410005), the Excellent Young Teachers Program of M0E, P.R.C. ([2003]355#), and the China Scholarship programs. N.D. and P.C.S. acknowledge the financial support provided by the MITACS Network of Centres of Excellence, Ballard Power Systems and the Canada Research Chairs program.

References

[1] T. Berning, N. Djilali, J. Electrochem. Soc. 150 (2003) A1589–A1598.
[2] A. Taniguchi, T. Akita, K. Yasuda, Y. Miyazaki, J. Power Sources 130 (2004) 42–49.
[3] K. Tuber, D. Pocza, C. Hebling, J. Power Sources 124 (2003) 403–414.
[4] X.G. Yang, F.Y. Zhang, A.L. Lubawy, C.Y. Wang, Electrochem. Solid State Lett. 7 (2004) A408–A411.
[5] F.Y. Zhang, X.G. Yang, C.Y. Wang, J. Electrochem. Soc. 153 (2006) A225–A232.
[6] M.M. Mench, C.Y. Wang, M. Ishikawa, J. Electrochem. Soc. 150 (2003) A1052–A1059.
[7] K. Sugiura, M. Nakata, T. Yodo, Y. Nishiguchi, M. Yamauchi, Y. Itoh, J. Power Sources 145 (2005) 526–533.
[8] F.B. Weng, A. Su, C.Y. Hsu, C.Y. Lee, J. Power Sources 157 (2006) 674–680.
[9] R. Satija, D.L. Jacobson, M. Arif, S.A. Werner, J. Power Sources 129 (2004) 238–245.
[10] D. Kramer, J.B. Zhang, R. Shimoi, E. Lehmann, A. Wokaun, K. Shinohara, G.G. Scherer, Electrochim. Acta 50 (2005) 2603–2614.
[11] M.A. Hickner, N.P. Siegel, K.S. Chen, D.N. McBrayer, D.S. Hussey, D.L. Jacobson, M. Arif, J. Electrochem. Soc. 153 (2006) A902–A908.
[12] N. Pekula, K. Heller, P.A. Chuang, A. Turhan, M.M. Mench, J.S. Brenizer, K. Unlu, Nucl. Instrum. Methods Phys. Res. Sect. a—Accelerators Spectrometers Detectors Assoc. Equipment 542 (2005) 134–141.

[13] A. Hakenjos, H. Muenter, U. Wittstadt, C. Hebling, J. Power Sources 131 (2004) 213–216.
[14] K.W. Feindel, L.P.A. LaRocque, D. Starke, S.H. Bergens, R.E. Wasylishen, J. Am. Chem. Soc. 126 (2004) 11436–11437.
[15] S. Tsushima, K. Teranishi, S. Hirai, Electrochem. Solid State Lett. 7 (2004) A269–A272.
[16] S. Litster, D. Sinton, N. Djilali, J. Power Sources 154 (2006) 95–105.
[17] A. Bazylak, D. Sinton, Z.S. Liu, N. Djilali, J. Power Sources 163 (2007) 784–792.
[18] Z.H. Wang, C.Y. Wang, K.S. Chen, J. Power Sources 94 (2001) 40–50.
[19] U. Pasaogullari, C.Y. Wang, J. Electrochem. Soc. 151 (2004) A399–A406.
[20] J.J. Baschuk, X.H. Li, J. Power Sources 86 (2000) 181–196.
[21] N.P. Siegel, M.W. Ellis, D.J. Nelson, M.R. von Spakovsky, J. Power Sources 128 (2004) 173–184.
[22] L.X. You, H.T. Liu, Int. J. Heat Mass Transf. 45 (2002) 2277–2287.
[23] M.R. Hu, A.Z. Gu, M.H. Wang, X.J. Zhu, L.J. Yu, Energy Convers. Manage. 45 (2004) 1861–1882.
[24] T.E. Springer, T.A. Zawodzinski, S. Gottesfeld, J. Electrochem. Soc. 138 (1991) 2334–2342.
[25] P.C. Sui, N. Djilali, ASME J. Fuel Cell Sci. Technol. 2 (2005) 149–155.
[26] J. Fimrite, H. Struchtrup, N. Djilali, J. Electrochem. Soc. 152 (2005) A1804–A1814.
[27] K.S. Chen, M.A. Hickner, D.R. Noble, Int. J. Energy Res. 29 (2005) 1113–1132.
[28] K. Jiao, B. Zhou, P. Quan, J. Power Sources 157 (2006) 226–243.
[29] P. Quan, B. Zhou, A. Sobiesiak, Z.S. Liu, J. Power Sources 152 (2005) 131–145.
[30] E.C. Kumbur, K.V. Sharp, M.M. Mench, J. Power Sources 161 (2006) 333–345.
[31] X. Zhu, P.C. Sui, N. Djilali, Microfluid. Nanofluid. (2007), doi:10.1007/s10404-007-0209-9, in press.
[32] C.W. Hirt, B.D. Nichols, J. Comput. Phys. 39 (1981) 201–225.
[33] J. Martin, P. Oshkai, N. Djilali, J. Fuel Cell Sci. Technol. 2 (2005) 70–80.
[34] J.G. Pharoah, Int. J. Green Energy 2 (2005) 421–438.
[35] FLUENT 6.2 User's Guide, 2006.
[36] J.U. Brackbill, D.B. Kothe, C. Zemach, J. Comput. Phys. 100 (1992) 335–354.
[37] J. Chakraborty, N. Verma, R.P. Chhabra, Chem. Eng. Process. 43 (2004) 1529–1537.